molecules

MDPI

Article

# Reduced Graphene Oxide-Supported $SrV_4O_9$ Microflowers with Enhanced Electrochemical Performance for Sodium-Ion Batteries

**Guangming Li [1,2], Yifan Li [2], Yi Zhang [2], Shuguo Lei [2], Jiwei Hou [2,*], Huiling Lu [3] and Baizeng Fang [4,*]**

1 CNG Wind Energy Co., Ltd., Beijing 100160, China
2 School of Physical and Mathematical Science, Nanjing Tech University, Nanjing 211816, China
3 School of Chemistry and Chemical Engineering, Jiangsu University, Zhenjiang 212013, China; lhl@ujs.edu.cn
4 School of Chemical Engineering and Energy Technology, Dongguan University of Technology, Dongguan 523808, China
* Correspondence: jwhou@njtech.edu.cn (J.H.); baizengfang@163.com (B.F.)

**Abstract:** Sodium-ion batteries (SIBs) have received considerable attention in recent years. Anode material is one of the key factors that determine SIBs' electrochemical performance. Current commercial hard carbon anode shows poor rate performance, which greatly limits applications of SIBs. In this study, a novel vanadium-based material, $SrV_4O_9$, was proposed as an anode for SIBs, and its $Na^+$ storage properties were studied for the first time. To enhance the electrical conductivity of $SrV_4O_9$ material, a microflower structure was designed and reduced graphene oxide (rGO) was introduced as a host to support $SrV_4O_9$ microflowers. The microflower structure effectively reduced electron diffusion distance, thus enhancing the electrical conductivity of the $SrV_4O_9$ material. The rGO showed excellent flexibility and electrical conductivity, which effectively improved the cycling life and rate performance of the $SrV_4O_9$ composite material. As a result, the $SrV_4O_9$@rGO composite showed excellent electrochemical performance (a stable capacity of 273.4 mAh $g^{-1}$ after 200 cycles at 0.2 A $g^{-1}$ and a high capacity of 120.4 mAh $g^{-1}$ at 10.0 A $g^{-1}$), indicating that $SrV_4O_9$@rGO composite can be an ideal anode material for SIBs.

**Keywords:** $SrV_4O_9$; rGO; sodium-ion batteries; anode; electrochemical performance

check for updates

**Citation:** Li, G.; Li, Y.; Zhang, Y.; Lei, S.; Hou, J.; Lu, H.; Fang, B. Reduced Graphene Oxide-Supported $SrV_4O_9$ Microflowers with Enhanced Electrochemical Performance for Sodium-Ion Batteries. *Molecules* **2024**, *29*, 2704. https://doi.org/10.3390/molecules29112704

Academic Editors: Jianjun Zhang and Liwen Tan

Received: 12 May 2024
Revised: 29 May 2024
Accepted: 31 May 2024
Published: 6 June 2024



## 1. Introduction

The widespread use of fossil fuels has created several energy and environmental issues that threaten the sustainable development of human society. It is important to develop renewable energy to overcome environmental problems. However, renewable energy—solar, tidal, and wind—is generally unstable, and requires the support of energy storage systems. Among various energy storage systems, lithium-ion batteries (LIBs) are widely used in consumer electronics and power tools due to their high energy density, environmental friendliness, and no memory effect [1–8]. However, due to required expensive rare metals, such as lithium and cobalt, LIBs cannot well meet the demand for widespread energy storage.

In recent years, sodium-ion batteries (SIBs) have received considerable attention from international researchers due to their many advantages: (1) sodium resources are abundant and widely distributed [9–11], (2) SIBs have similar working mechanisms to LIBs so they can be manufactured by the same technologies as LIBs [12], (3) to achieve the same ionic conductivity, the concentration of sodium salts in electrolytes is lower than that of lithium salts, resulting in lower cost, (4) aluminum foil can be used as the current collector for the anode in SIBs because $Na^+$ does not react with aluminum, further reducing the cost, and (5) SIBs have high safety performance due to higher internal resistance compared to LIBs. Therefore, SIBs are considered as an alternative to LIBs in some areas.

The anode material is one of the key factors determining the electrochemical performance of batteries [13–18]. The main anode materials for SIBs include carbon materials,

alloy materials, transition metal oxides, and organic compounds. Among them, hard carbons are the most cost effective, making them promising for industrial application. However, the rate performance of hard carbons is poor, which limits their applications [19,20]. Therefore, it is essential to develop anode materials with high $Na^+$ diffusion coefficient for SIBs. Vanadium-based materials have been widely studied as anode materials for SIBs [21,22] due to several advantages. Firstly, they exhibit high capacity due to the multivalent nature of vanadium. Secondly, they have a high $Na^+$ diffusion coefficient. Finally, vanadium resources are abundant and environmentally friendly. To date, a novel vanadium-based material ($SrV_4O_9$) has been prepared and has shown excellent $Zn^{2+}$ storage performance [23]. However, research into $SrV_4O_9$ as an anode material for SIBs has not been reported.

In this work, the $Na^+$ storage performance of $SrV_4O_9$ material was studied to enhance the electrical conductivity of $SrV_4O_9$ material, and a microflower structure was designed. Reduced graphene oxide (rGO) was then introduced as a host to support $SrV_4O_9$ microflowers. The microflower structure effectively reduced electron diffusion distance, thus enhancing the electrical conductivity of the $SrV_4O_9$ material. In addition, the rGO showed excellent flexibility and electrical conductivity, which can effectively improve the cycling life and rate performance of $SrV_4O_9$ material. As a result, the $SrV_4O_9$@rGO anode exhibited excellent cycling performance and remarkable rate performance.

## 2. Results and Discussion

The preparation scheme for $SrV_4O_9$@rGO is shown in Figure 1. The $SrV_4O_9$@rGO shows a microflower structure. The mechanism of formation of the $SrV_4O_9$ flower-like structure involved a combination of factors, including precursor and growth conditions. First, $Sr(OH)_2 \cdot 8H_2O$ and $V_2O_5$ were dissolved in a solvent and heated at 200 °C for 48 h to form a precursor cluster. The precursor was then heated to 450 °C under argon and held for 5 h. During this process, many branches were formed on the cluster and then grew to eventually form hierarchical structures with intricate morphologies resembling flowers.

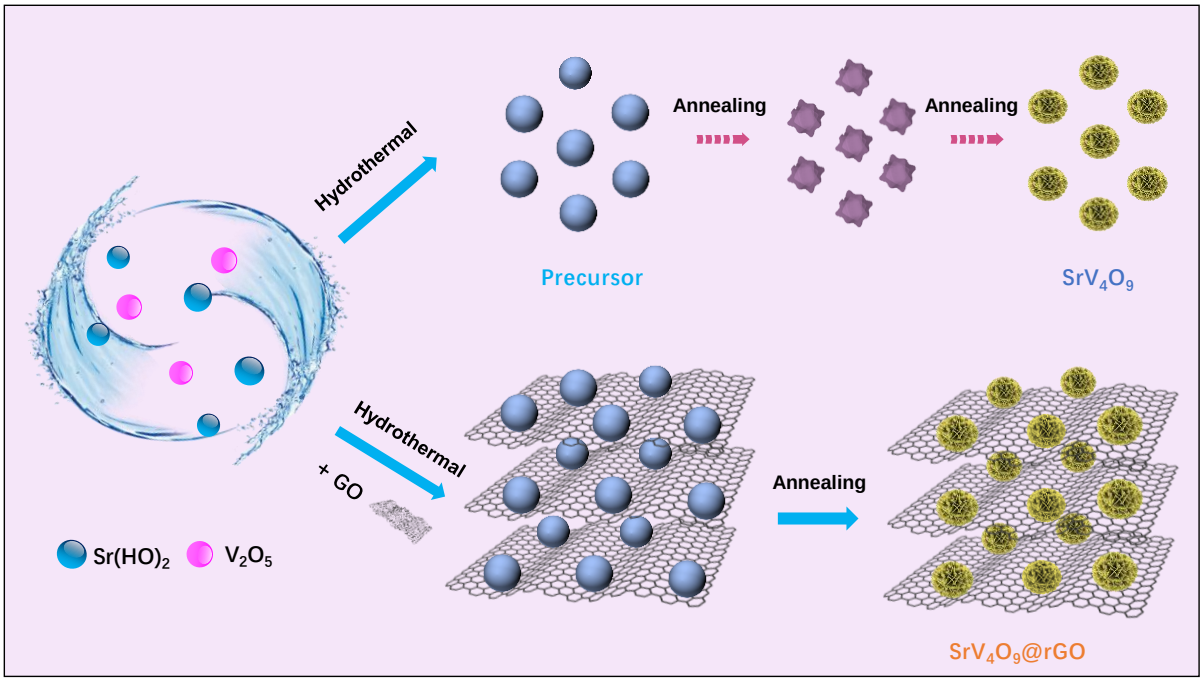


**Figure 1.** The preparation scheme for $SrV_4O_9$ and the $SrV_4O_9$@rGO composite.

The structure of the $SrV_4O_9$@rGO composite was investigated by XRD. As shown in Figure 2a, peaks at 16.8°, 29.2°, 33.8°, 35.8°, 48.7°, 52.5°, 57.7°, and 71.1° can be assigned to the (001), (121), (310), (102), (240), (322), (501), and (620) planes of $SrV_4O_9$ (JCPDS No. 70-

4468) [23], respectively. Note that rGO diffraction peaks were observed at 26.8° and 42.4°. However, the intensity of the rGO diffraction peaks was weak due to the dense coating of $SrV_4O_9$ on the rGO. To probe the structure of the $SrV_4O_9$@rGO composite, Raman spectroscopy experiments were performed. As seen in Figure 2b, peaks at 148, 292, 380, 524, 682, and 992 $cm^{-1}$ can be attributed to $SrV_4O_9$ [23]. For the $SrV_4O_9$@rGO composite, two additional broad peaks at 1348 and 1578 $cm^{-1}$ corresponded to the D-band and G-band of the rGO, respectively [24,25]. The $SrV_4O_9$@rGO composite was further tested by nitrogen adsorption–desorption experiments to characterize its porosity and specific surface area (Figure 2c,d). The $SrV_4O_9$@rGO composite exhibited a Type I isotherm, indicating abundant micro/mesopores in its structure [26,27]. The specific surface area of the $SrV_4O_9$@rGO composite was 41.4 $m^2$ $g^{-1}$. Figure 2d reveals that the average pore size of the $SrV_4O_9$@rGO composite was 17.2 nm, further confirming its porous structure.

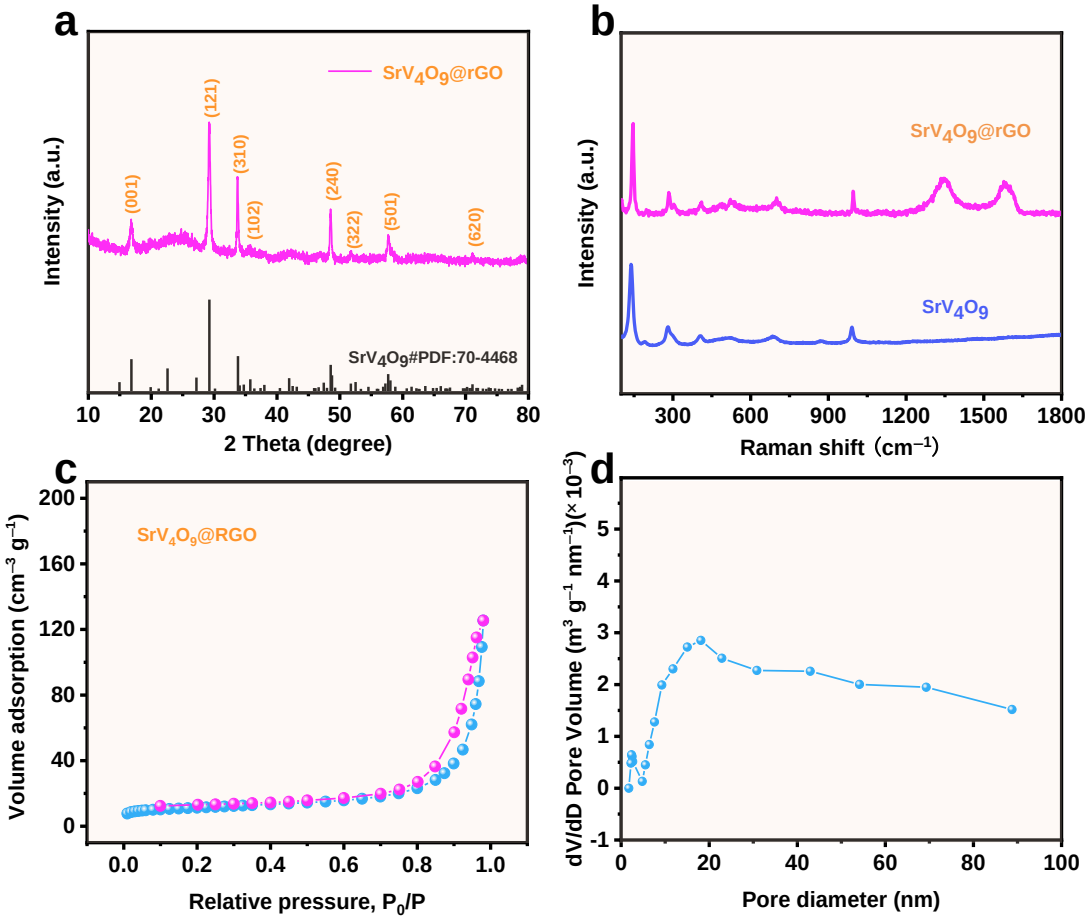


**Figure 2.** (**a**) XRD pattern of the $SrV_4O_9$@rGO composite. (**b**) Raman spectra of $SrV_4O_9$ and $SrV_4O_9$@rGO. (**c**) $N_2$ adsorption–desorption isotherms of $SrV_4O_9$@rGO. (**d**) Pore size distribution of $SrV_4O_9$@rGO.

To study its morphology, the $SrV_4O_9$@rGO composite was characterized using SEM and TEM. As shown in Figure 3a,b, the $SrV_4O_9$@rGO composite exhibited a three-dimensional porous spherical structure with a diameter of ~6 μm in which flexible rGO coated $SrV_4O_9$ microflowers. Figure 3c shows that $SrV_4O_9$ had a regular micrometer-scale flower-like structure with an average diameter of ~1 μm consisting of porous ultrathin nanosheets with a thickness of ~50 nm (Figure 3d). TEM images (Figure 3e,f) confirmed the three-dimensional porous structure of the $SrV_4O_9$@rGO composite. The porous nanostructure increases the contact area between the active material and the electrolyte and effectively reduces the ion diffusion distance, thus improving ion transport efficiency [28–32]. In addition, the porous nanostructure provides sufficient buffering space for

volume expansion during cycling processes, effectively enhancing cycling stability [33–38]. As shown in Figure 3g–j, Sr, V, O, and C were uniformly dispersed in the $SrV_4O_9$@rGO composite, indicating that $SrV_4O_9$ was uniformly loaded in rGO.

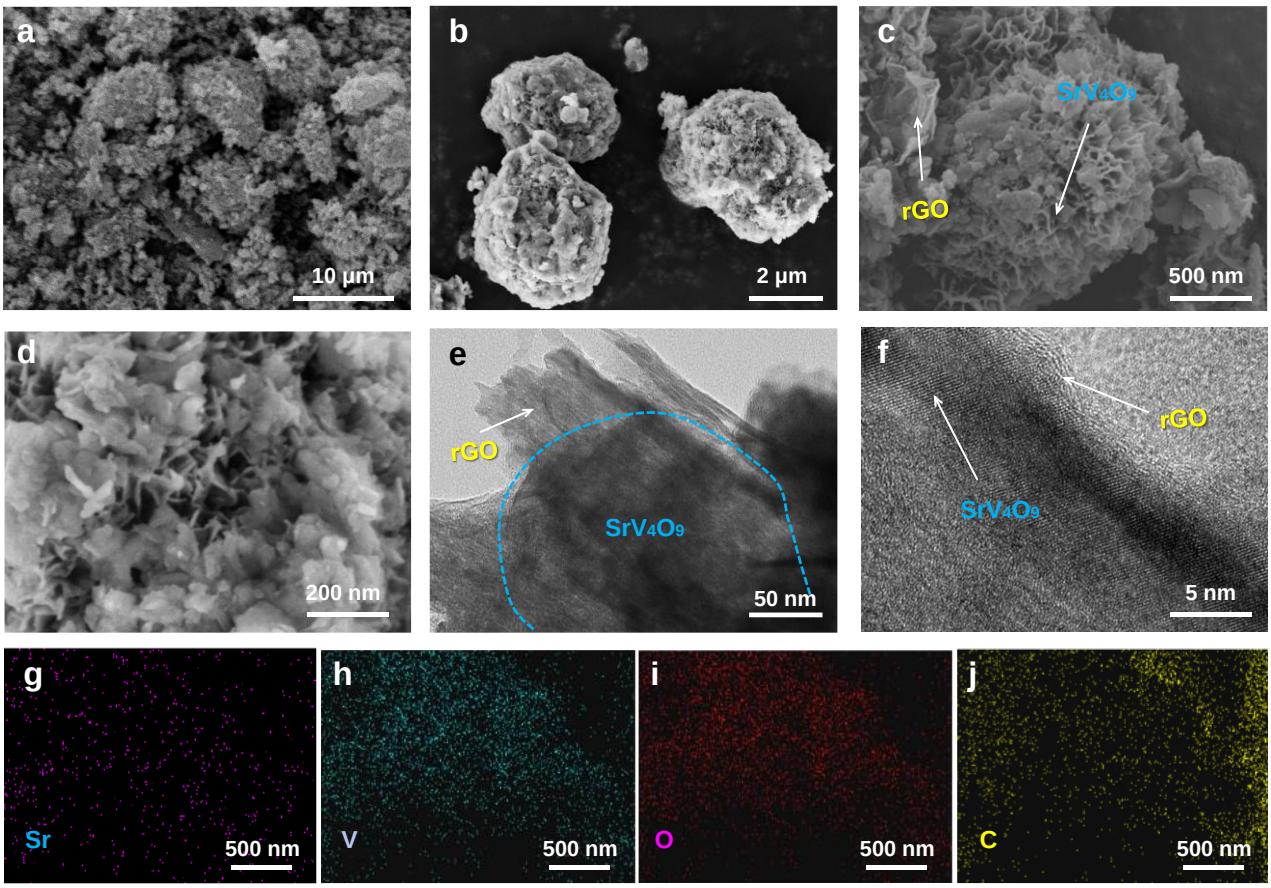


**Figure 3.** (**a**–**d**) SEM images of the $SrV_4O_9$@rGO composite. (**e**,**f**) TEM images of the $SrV_4O_9$@rGO composite. (**g**–**j**) EDS elemental mapping of Sr, V, O, and C.

XPS is a powerful analytical technique for characterizing the chemical composition and oxidation state of materials. The importance of XPS lies in its ability to provide detailed information about the chemical composition of the $SrV_4O_9$@rGO composite at the atomic level. Figure 4a shows the XPS survey spectrum of the $SrV_4O_9$@rGO composite, which shows the photoemission characteristics of Sr, V, O, and C. The high-resolution spectrum of Sr 3d (Figure 4b) can be deconvoluted into $Sr^{2+}$ $3d_{5/2}$ (135.6 eV) and $Sr^{2+}$ $3d_{3/2}$ (133.2 eV) [23]. The V 2p high-resolution spectrum (Figure 4c) can be deconvoluted into $V^{4+}$ $2p_{1/2}$ (523.6 eV) and $V^{4+}$ $2p_{3/2}$ (516.6 eV) [39,40]. The high-resolution spectrum of O 1s (Figure 4d) exhibits two peaks, at 531.6 eV and 530.4 eV; the peak at 530.4 eV corresponds to the bonding of adsorbed oxygen on the surface of the $SrV_4O_9$@rGO composite with Sr and V, denoted as Sr–O–V [23], while the peak at 531.8 eV was likely due to the presence of $H_2O$. As shown in Figure 4e, the high-resolution spectrum of C 1s reveals distinct peaks at 285.6 eV and 284.8 eV, corresponding to C–O and C–C bonds, respectively [41,42].

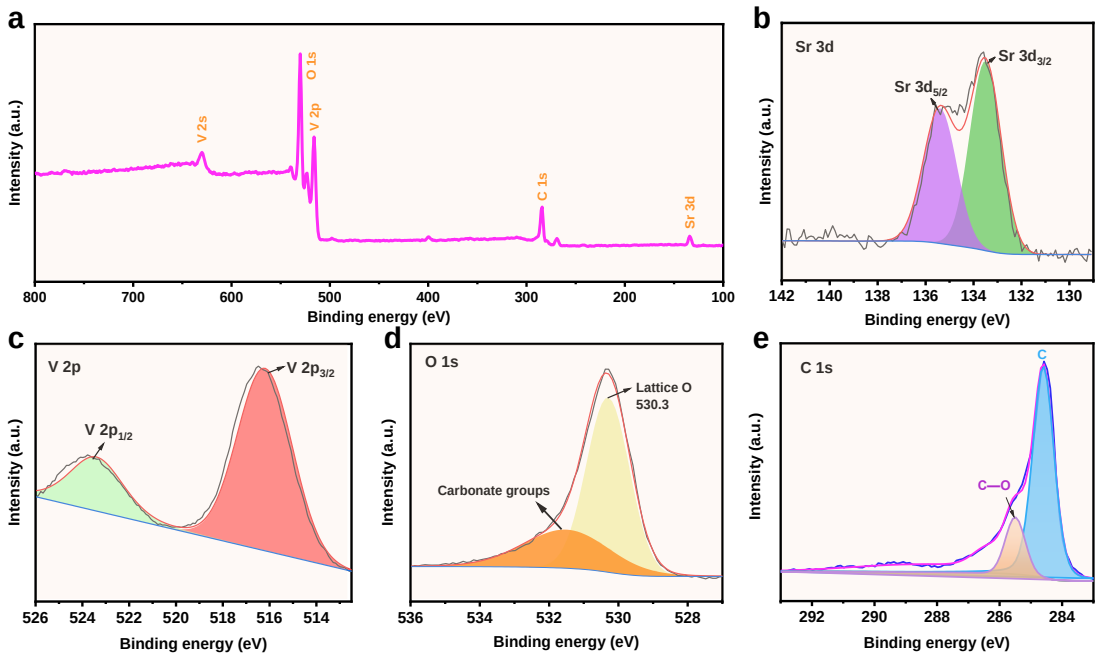


**Figure 4.** (**a**) The XPS survey spectrum of the $SrV_4O_9$@rGO composite. (**b**) The high-resolution spectrum of Sr 3d. (**c**) The high-resolution spectrum of V 2p. (**d**) The high-resolution spectrum of O 1s. (**e**) The high-resolution spectrum of C 1s.

Figure 5a,b compare the CV curves of $SrV_4O_9$-based and $SrV_4O_9$@rGO-based electrodes for the first three cycles between 0.01 and 3.0 V at a scan rate of 0.1 mV $s^{-1}$. All CV curves exhibited two reduction peaks and one oxidation peak. Two reduction peaks appeared at ~0.75 V and ~0.45 V, representing the penetration of sodium ions into $SrV_4O_9$. A weak and broad oxidation peak at around 1.48 V might correspond to the oxidation reaction of V. And the CV curves of the second and third cycles showed a high degree of overlap, indicating good reversibility of the electrochemical reactions. It is worth noting that the peak current densities of the oxidation–reduction peaks of the $SrV_4O_9$@rGO-based electrode (Figure 5b) were higher than those of the $SrV_4O_9$-based electrode (Figure 5a), indicating the improved electron/ion transport kinetics of the $SrV_4O_9$@rGO composite facilitated by rGO and more dispersed $SrV_4O_9$. The cycling performances of the $SrV_4O_9$-based and $SrV_4O_9$@rGO-based electrodes at 0.2 A $g^{-1}$ are shown in Figure 5c. The $SrV_4O_9$@rGO composite showed a high initial reversible capacity of 284.4 mAh $g^{-1}$ and maintained a stable capacity of 273.4 mAh $g^{-1}$ after 200 cycles, with an ultra-high capacity retention of 96.1%. For the $SrV_4O_9$ electrode, the capacity after 200 cycles was only 142.5 mAh $g^{-1}$. The excellent cycling performance can be attributed to the super aspect ratio of the porous microflower structure, which facilitated ion transfer. The introduction of rGO increased the specific surface area involved in the reaction, providing more reaction sites. The galvanostatic charge–discharge (GCD) curves of the $SrV_4O_9$@rGO electrode are shown in Figure 5d. These GCD curves show a high degree of overlap, indicating excellent cycling performance of the $SrV_4O_9$@rGO electrode. To characterize the positive effect of rGO on $SrV_4O_9$, an EIS test was performed. Figure S1 shows Nyquist plots for $SrV_4O_9$ and $SrV_4O_9$@rGO electrodes in the initial state and the $SrV_4O_9$@rGO electrode after 200 cycles. The $SrV_4O_9$@rGO electrode exhibited a smaller charge transfer resistance than the $SrV_4O_9$ electrode in the initial state, indicating that rGO improved the rate of $Na^+$ transfer. A comparison between the initial and cycled electrodes revealed a significant decrease in impedance for the $SrV_4O_9$@rGO electrode after 200 cycles at 0.2 A $g^{-1}$ due to the considerably enhanced ion and electron transfer in the electrode. The SEM image of the $SrV_4O_9$@rGO electrode after 200 cycles (Figure S2) revealed that the $SrV_4O_9$@rGO electrode had good structural stability after electrochemical testing. The $SrV_4O_9$@rGO electrode

also demonstrated excellent rate performance (Figure 5e). At 0.1, 0.2, 0.5, 1.0, 2.0, 5.0, and 10.0 A $g^{-1}$, the specific capacities of the $SrV_4O_9$@rGO electrode remained at 287.1, 268.5, 250.4, 228.7, 209.6, 168.2, and 120.4 mAh $g^{-1}$, respectively, which were significantly higher than those of the $SrV_4O_9$ electrode (149.4, 119.0, 85.6, 69.2, 47.3, 23.1, and 7.7 mAh $g^{-1}$, respectively). The cycling performance of the $SrV_4O_9$@rGO composite at a high rate (1 A $g^{-1}$) was also tested, and results are shown in Figure S3. The $SrV_4O_9$@rGO composite delivered an initial reversible discharge capacity of 278.3 mAh $g^{-1}$ at 1.0 A $g^{-1}$. The capacity decreased slightly to 265.7 mAh $g^{-1}$ after 310 cycles, demonstrating good cycling performance at a high rate. The improved electrochemical performance of the $SrV_4O_9$@rGO composite can be attributed to the large aspect ratio of the composite and improved electrical conductivity [43,44] (Figure 5f).

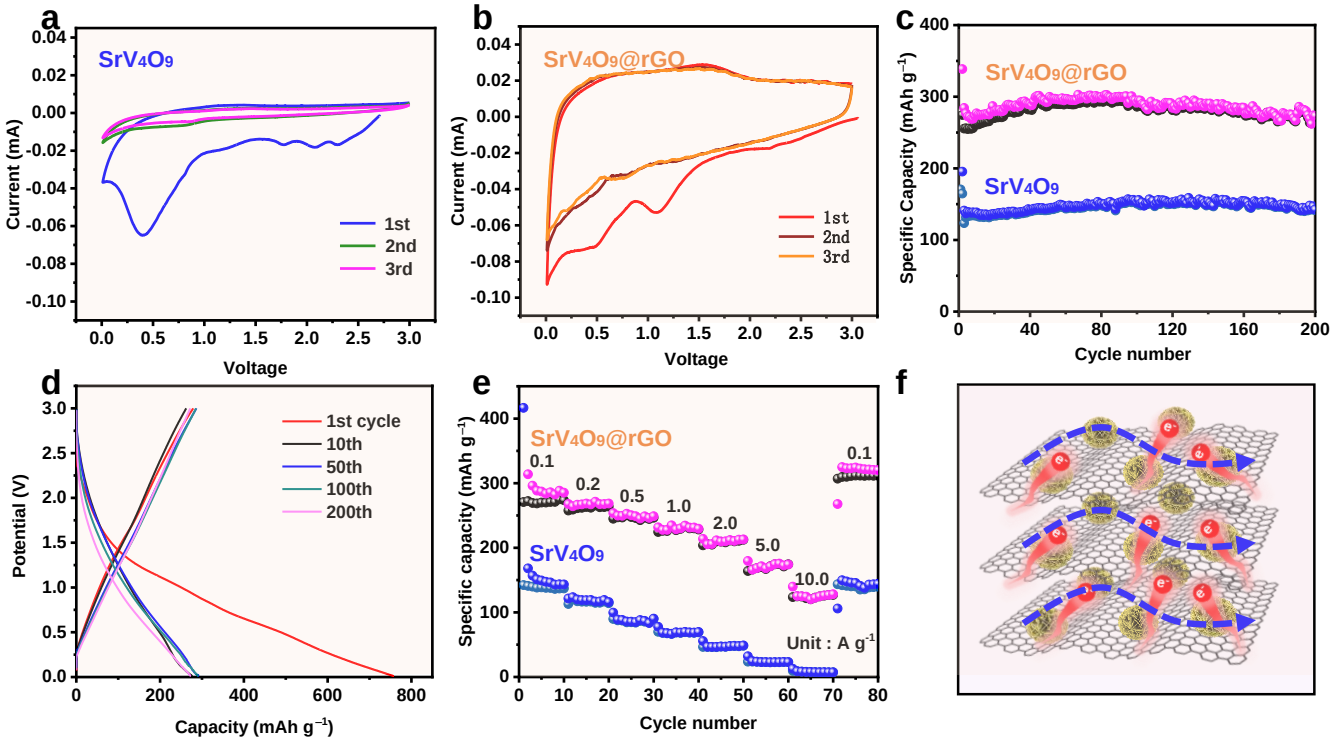


**Figure 5.** (**a**) CV curves of the $SrV_4O_9$-based electrode for the initial three cycles between 0.01 and 3.0 V at a scan rate of 0.1 mV $s^{-1}$. (**b**) CV curves of $SrV_4O_9$@rGO-based electrodes for the initial three cycles between 0.01 and 3.0 V at a scan rate of 0.1 mV $s^{-1}$. (**c**) Cycling performance of the $SrV_4O_9$-based electrode and the $SrV_4O_9$@rGO-based electrode at 0.2 A $g^{-1}$. (**d**) Voltage profiles of the $SrV_4O_9$@rGO-based electrode at 0.2 A $g^{-1}$. (**e**) Rate performance of the $SrV_4O_9$-based electrode and the $SrV_4O_9$@rGO-based electrode. (**f**) Schematic illustration of the reaction mechanism of the $SrV_4O_9$@rGO-based electrode.

## 3. Experimental Section

### *3.1. Materials*

All reagents were directly used after purchase. $Sr(OH)_2{\cdot}8H_2O$, $C_3H_8O_3$, $V_2O_5$, and $H_2O_2$ were purchased from Sigma-Aldrich (St. Louis, MO, USA). GO was provided by Nanjing XFNANO Materials Tech Co., Ltd. (Nanjing, China).

### *3.2. Synthesis of $SrV_4O_9$@rGO Composite and $SrV_4O_9$*

The $SrV_4O_9$@rGO composite was prepared using the hydrothermal annealing method. First, 1 mmol of $Sr(OH)_2{\cdot}8H_2O$ was dissolved in a mixed solution consisting of 10 mL of deionized water and 10 mL of $C_3H_8O_3$. Next, 2 mmol (0.364 g) of $V_2O_5$ and 0.05 g of GO were added to a mixed solution consisting of 10 mL of deionized water and 5 mL of $H_2O_2$ (30%) and stirred for 1 h, and was then slowly added to the $Sr(OH)_2{\cdot}8H_2O$ solution,

followed by stirring for 2 h. The mixed solution was transferred to a hydrothermal reactor and heated in an oven at 200 °C for 48 h. After cooling to room temperature, the precipitate was collected after several washes with deionized water and ethanol. The collected material was then dried in a vacuum oven at 80 °C for 24 h. Finally, the collected material was heated to 450 °C at a heating rate of 5 °C $min^{-1}$ in a tube furnace under argon and then held for 5 h to obtain $SrV_4O_9$@rGO. For comparison, $SrV_4O_9$ was prepared using the same procedures without the addition of GO.

### *3.3. Characterization*

X-ray diffraction (XRD, Rigaku MiniFlexll, Rigaku Corporation, Tokyo, Japan) patterns were collected from 10° to 80° using Cu K$\alpha$ radiation ($\lambda$ = 1.5408 Å). X-ray photoelectron spectra (XPS, Thermo Scientific K-Alpha, Waltham, MA, USA) surveys and specific patterns were obtained with an Al K$\alpha$ X-ray source. The structures of SrV4O9 and $SrV_4O_9$@rGO were further examined by Raman spectroscopy (Thermo Fisher DXR2xi). Morphologies of $SrV_4O_9$ and the $SrV_4O_9$@rGO composite were analyzed by scanning electron microscopy (SEM, JEOL JSM-7800F Field Emission, Manufacturer JEOL Ltd., Tokyo, Japan) with EDS mapping (JEOL JSM-7100F, Manufacturer JEOL Ltd., Tokyo, Japan) and transmission electron microscopy (TEM, JEOL JEM, 1011, Manufacturer JEOL Ltd., Tokyo, Japan). $N_2$ adsorption–desorption isotherms were measured on an Autosorb-iQ instrument (Quantachrome, Anton Paar acquired Quantachrome Instruments, Inc., Boynton Beach, FL, USA).

### *3.4. Electrochemical Measurements*

To prepare the working electrode, $SrV_4O_9$ or the $SrV_4O_9$@rGO composite (70 wt%) was combined with acetylene black (20 wt%) and polyvinylidene difluoride (10 wt%) in 1-methyl-2-pyrrolidone to form a uniform slurry. The slurry was then coated onto copper foil and dried at 80 °C for 12 h. The loading density of the active materials was about 1.2–1.5 mg $cm^{-2}$. For electrochemical performance testing, a CR2025 coin cell was assembled with $SrV_4O_9$ or the $SrV_4O_9$@rGO composite as the working electrode, Na foil as the counter electrode, and glass fiber membrane (Whatman GF/A) as the separator. The electrolyte was 1 M $NaClO_4$ dissolved in ethylene carbonate/dimethyl carbonate (EC/DMC, 1:1 by volume) with 5 wt% of fluorodimethylene carbonate (FEC) as an additive. Galvanostatic charge–discharge curves and cycling performance evaluations were performed on a LAND battery test system in the range of 0.01–3.0 V. Cyclic voltammetry (CV) tests were performed using the CHI660e electrochemical workstation.

## 4. Conclusions

In summary, an rGO-supported $SrV_4O_9$ composite was synthesized as an anode material for SIBs. The $SrV_4O_9$ had a regular micrometer-scale flower-like structure consisting of porous ultrathin nanosheets with a thickness of ~50 nm, which was coated with rGO to form a three-dimensional porous spherical structure. The porous nanostructure increased the contact area between $SrV_4O_9$@rGO and the electrolyte and effectively reduced the ion diffusion distance, thus improving ion transport efficiency. In addition, the porous nanostructure reduced $SrV_4O_9$ aggregation and provided sufficient buffering space for volume expansion during cycling processes, effectively improving cycling stability. Therefore, the $SrV_4O_9$@rGO composite showed a high initial reversible capacity of 284.4 mAh $g^{-1}$ at 0.2 A $g^{-1}$ and retained a stable capacity of 273.4 mAh $g^{-1}$ after 200 cycles with an ultra-high capacity retention of 96.1%. At 0.1, 0.2, 0.5, 1.0, 2.0, 5.0, and 10.0 A $g^{-1}$, the specific capacities of the $SrV_4O_9$@rGO electrode remained at 287.1, 268.5, 250.4, 228.7, 209.6, 168.2, and 120.4 mAh $g^{-1}$, respectively, demonstrating excellent rate performance.

**Supplementary Materials:** The following supporting information can be downloaded at https://www.mdpi.com/article/10.3390/molecules29112704/s1, Figure S1: Nyquist plots of the SrV4O9 and SrV4O9@rGO electrodes in the initial state and the SrV4O9@rGO electrode after 200 cycles; Figure S2: SEM image of the SrV4O9@rGO electrode after 200 cycles at 0.2 A g−1; Figure S3: Cycling performance of the SrV4O9@rGO composite after 200 cycles at 1 A $g^{-1}$.

**Author Contributions:** Writing—original draft preparation, G.L.; Conceptualization, Y.L.; Investigation, Y.Z. and S.L.; Funding acquisition, J.H.; Project administration, H.L.; Writing—review and editing, B.F. All authors have read and agreed to the published version of the manuscript.

**Funding:** The work was supported by the Foundation of Key Laboratory of Flexible Electronics of Zhejiang Province (No. 2023FE011).

**Institutional Review Board Statement:** Not applicable.

**Informed Consent Statement:** Not applicable.

**Data Availability Statement:** Data are available upon request from the corresponding authors.

**Conflicts of Interest:** Guangming Li was employed by CNG Wind Energy Co., Ltd. The remaining authors declare that the research was conducted in the absence of any commercial or financial relationships that could be construed as a potential conflict of interest.

## References

1. Gu, S.; Kong, J.; Fang, B. Comprehensive recycling of spent lithium-ion batteries cathodes and anodes via targeted electrochemical redox process. *Green Chem.* **2024**, *26*, 4484–4492. [CrossRef]
2. Li, J.; Xie, Q.; Zhao, Y.; Zhao, P.; Zhang, S.; Huang, W. Unveiling morphology evolution and performance enhancement of tin-doped $Co_3O_4$ porous nanoarrays anchored on stainless-steel mesh for advanced lithium-ion battery anodes. *J. Energy Storage* **2024**, *88*, 111605. [CrossRef]
3. Sun, R.; Qin, Z.; Li, Z.; Fan, H.; Lu, S. Binary zinc-cobalt metal-organic framework derived mesoporous $ZnCo_2O_4$@NC polyhedron as a high-performance lithium-ion battery anode. *Dalton Trans.* **2020**, *49*, 14237–14242. [CrossRef]
4. Guo, Y.; Zhang, X.; Jin, S.; Xia, Q.; Chang, Y.; Wang, L.; Zhou, A. Synthesis of $Mo_2C$ MXene with high electrochemical performance by alkali hydrothermal etching. *J. Adv. Ceram.* **2023**, *12*, 1889–1901. [CrossRef]
5. Fang, B.; Wang, Y.; Wang, H. Does an $LaCl_3$-based lithium superionic conductor work well for anode-free lithium metal batteries? *Matter* **2023**, *6*, 2508–2510. [CrossRef]
6. Li, J.; Lu, Y.; Quan, K.; Wu, L.; Feng, X.; Wang, W. One-pot cocrystallization of mononuclear and 1D cobalt (II) complexes based on flexible triclopyr and 2, 2′-bipyridine coligands: Structural analyses, conformation comparison, non-covalent interactions and magnetic properties. *J. Mol. Struct.* **2024**, *1297*, 136830. [CrossRef]
7. Song, M.; Liu, Y.; Hong, J.; Wang, X.; Huang, X. Boosting bidirectional conversion of polysulfide driven by the built-in electric field of $MoS_2$/MoP Mott–Schottky heterostructures in lithium–sulfur batteries. *J. Adv. Ceram.* **2023**, *12*, 1872–1888. [CrossRef]
8. Zheng, S.; Mo, L.; Chen, K.; Chen, A.-L.; Zhang, X.; Fan, X.; Lai, F.; Wei, Q.; Miao, Y.-E.; Liu, T.; et al. Precise Control of $Li^+$ Directed Transport via Electronegative Polymer Brushes on Polyolefin Separators for Dendrite-Free Lithium Deposition. *Adv. Funct. Mater.* **2022**, *32*, 2201430. [CrossRef]
9. Li, Z.; Sun, R.; Qin, Z.; Liu, X.; Wang, C.; Lu, S.; Zhang, Y.; Fan, H. Coupling of $ReS_2$ nanosheet arrays with hollow $NiCoS_4$ nanocubes enables ultrafast $Na^+$ diffusion kinetics and super $Na^+$ storage of a $NiCoS_4$@$ReS_2$ heterostructure. *Mater. Chem. Front.* **2021**, *5*, 7540–7547. [CrossRef]
10. Zhu, J.; He, Q.; Liu, Y.; Key, J.; Nie, S.; Wu, M.; Shen, P.K. Three-dimensional, hetero-structured, $Cu_3P$@C nanosheets with excellent cycling stability as Na-ion battery anode material. *J. Mater. Chem. A* **2019**, *7*, 16999–17007. [CrossRef]
11. Zhu, J.; Wei, P.; Zeng, Q.; Wang, G.; Wu, K.; Ma, S.; Shen, P.K.; Wu, X.-L. MnS@N,S Co-Doped Carbon Core/Shell Nanocubes: Sulfur-Bridged Bonds Enhanced Na-Storage Properties Revealed by In Situ Raman Spectroscopy and Transmission Electron Microscopy. *Small* **2020**, *16*, 2003001. [CrossRef] [PubMed]
12. Wang, Y.; Xiao, F.; Chen, X.; Xiong, P.; Lin, C.; Wang, H.-E.; Wei, M.; Qian, Q.; Chen, Q.; Zeng, L. Extraordinarily stable and wide-temperature range sodium/potassium-ion batteries based on 1D $SnSe_2$-SePAN composite nanofibers. *InfoMat* **2023**, *5*, e12467. [CrossRef]
13. Zhou, Y.; Yin, L.; Xiang, S.; Yu, S.; Johnson, H.M.; Wang, S.; Yin, J.; Zhao, J.; Luo, Y.; Chu, P.K. Unleashing the Potential of MXene-Based Flexible Materials for High-Performance Energy Storage Devices. *Adv. Sci.* **2024**, *11*, 2304874. [CrossRef] [PubMed]
14. Zhou, Y.-L.; Cheng, W.-N.; Bai, Y.-Z.; Hou, C.; Li, K.; Huang, Y.-A. Rise of flexible high-temperature electronics. *Rare Met.* **2023**, *42*, 1773–1777. [CrossRef]
15. Lin, H.; Lin, C.; Xiao, F.; He, L.; Xiong, P.; Luo, Y.; Hu, X.; Qian, Q.; Chen, Q.; Wen, Z.; et al. High-Performance Wide-pH Zn-Based Batteries via Electrode Interface Regulation with Valine Additive. *Adv. Funct. Mater.* **2024**, *34*, 2310486. [CrossRef]
16. Jia, Y.; Chen, S.; Shao, X.; Chen, J.; Fang, D.-L.; Li, S.; Mao, A.; Li, C. Synergetic effect of lattice distortion and oxygen vacancies on high-rate lithium-ion storage in high-entropy perovskite oxides. *J. Adv. Ceram.* **2023**, *12*, 1214–1227. [CrossRef]
17. Zhou, Y.; Wang, S.; Yin, J.; Wang, J.; Manshaii, F.; Xiao, X.; Zhang, T.; Bao, H.; Jiang, S.; Chen, J. Flexible Metasurfaces for Multifunctional Interfaces. *ACS Nano* **2024**, *18*, 2685–2707. [CrossRef] [PubMed]
18. Lin, C.; He, L.; Xiong, P.; Lin, H.; Lai, W.; Yang, X.; Xiao, F.; Sun, X.-L.; Qian, Q.; Liu, S.; et al. Adaptive Ionization-Induced Tunable Electric Double Layer for Practical Zn Metal Batteries over Wide pH and Temperature Ranges. *ACS Nano* **2023**, *17*, 23181–23193. [CrossRef] [PubMed]

19. Li, J.; Liu, M.; You, X.; Wang, J.; Feng, X. One-pot cocrystallization of 1D linear and zigzag cobalt (II) polymers assembled by triclopyr and 4, 4′-bipyridine: Structural comparison, conformational analysis, non-covalent interactions as well as the magnetic property of the latter. *Polyhedron* **2024**, *249*, 116791. [CrossRef]
20. Chen, Y.; Li, F.; Guo, Z.; Song, Z.; Lin, Y.; Lin, W.; Zheng, L.; Huang, Z.; Hong, Z.; Titirici, M.-M. Sustainable and scalable fabrication of high-performance hard carbon anode for Na-ion battery. *J. Power Sources* **2023**, *557*, 232534. [CrossRef]
21. Zhao, D.; Zhang, Z.; Ren, J.; Xu, Y.; Xu, X.; Zhou, J.; Gao, F.; Tang, H.; Liu, S.; Wang, Z.; et al. $Fe_2VO_4$ nanoparticles on rGO as anode material for high-rate and durable lithium and sodium ion batteries. *Chem. Eng. J.* **2023**, *451*, 138882. [CrossRef]
22. Wang, C.; Wang, Z.; Zhao, D.; Ren, J.; Liu, S.; Tang, H.; Xu, P.; Gao, F.; Yue, X.; Yang, H.; et al. Core–Shell $Co_2VO_4$/Carbon Composite Anode for Highly Stable and Fast-Charging Sodium-Ion Batteries. *ACS Appl. Mater. Interfaces* **2021**, *13*, 55020–55028. [CrossRef] [PubMed]
23. Yang, S.; Zhang, Y.; Du, Y.; Wang, Z.; Song, B.; Wang, X. $SrV_4O_9$ microflowers as high performance cathode for aqueous zinc-ion battery. *Mater. Lett.* **2023**, *331*, 133535. [CrossRef]
24. Xia, P.; Li, S.; Yuan, L.; Jing, S.; Peng, X.; Lu, S.; Zhang, Y.; Fan, H. Encapsulating CoRu alloy nanocrystals into nitrogen-doped carbon nanotubes to synergistically modify lithium-sulfur batteries separator. *J. Membr. Sci.* **2024**, *694*, 122395. [CrossRef]
25. Wu, S.; Yang, W.; Liu, Z.; Li, Y.; Fan, H.; Zhang, Y.; Zeng, L. Organic polymer coating induced multiple heteroatom-doped carbon framework confined $Co_{1-x}S$@NPSC core-shell hexapod for advanced sodium/potassium ion batteries. *J. Colloid Interface Sci.* **2024**, *660*, 97–105. [CrossRef] [PubMed]
26. Gao, F.; Yue, X.-A.; Xu, X.-Y.; Xu, P.; Zhang, F.; Fan, H.-S.; Wang, Z.-L.; Wu, Y.-T.; Liu, X.; Zhang, Y. A N/Co co-doped three-dimensional porous carbon as cathode host for advanced lithium–selenium batteries. *Rare Met.* **2023**, *42*, 2670–2678. [CrossRef]
27. Xu, F.; Li, S.; Jing, S.; Peng, X.; Yuan, L.; Lu, S.; Zhang, Y.; Fan, H. Cobalt-vanadium sulfide yolk-shell nanocages from surface etching and ion-exchange of ZIF-67 for ultra-high rate-capability sodium ion battery. *J. Colloid Interface Sci.* **2024**, *660*, 907–915. [CrossRef] [PubMed]
28. Xu, Y.; Yu, S.; Yin, Y.; Bi, L. Taking advantage of Li-evaporation in $LiCoO_2$ as cathode for proton-conducting solid oxide fuel cells. *J. Adv. Ceram.* **2022**, *11*, 1849–1859. [CrossRef]
29. Qu, Y.-P.; Zhou, Y.-L.; Luo, Y.; Liu, Y.; Ding, J.-F.; Chen, Y.-L.; Gong, X.; Yang, J.-L.; Peng, Q.; Qi, X.-S. Universal paradigm of ternary metacomposites with tunable epsilon-negative and epsilon-near-zero response for perfect electromagnetic shielding. *Rare Met.* **2024**, *43*, 796–809. [CrossRef]
30. Chen, X.; Zhou, W.; Wang, F.; Wu, H.; Zhong, S.; Li, B. Meliorative dielectric properties in core@double-shell structured Al@$Al_2O_3$@PDA/PVDF nanocomposites via decoupling the intra-particle polarization and inter-particle polarization. *Mater. Today Energy* **2024**, *41*, 101543. [CrossRef]
31. Sun, G.; Yang, D.; Zhang, Z.; Wang, Y.; Lu, W.; Feng, M. Oxygen vacancy-rich $MoO_3$ nanorods as photocatalysts for photo-assisted Li–$O_2$ batteries. *J. Adv. Ceram.* **2023**, *12*, 747–759. [CrossRef]
32. Wang, F.; Zhou, W.; He, Y.; Lv, Y.; Wang, Y.; Wang, Z. Synergetic improvement of dielectric properties and thermal conductivity in Zn@ZnO/carbon fiber reinforced silicone rubber dielectric elastomers. *Compos. Part A Appl. Sci. Manuf.* **2024**, *181*, 108129. [CrossRef]
33. Chen, J.; Yang, Y.; Yu, S.; Zhang, Y.; Hou, J.; Yu, N.; Fang, B. MOF-Derived Nitrogen-Doped Porous Carbon Polyhedrons/Carbon Nanotubes Nanocomposite for High-Performance Lithium–Sulfur Batteries. *Nanomaterials* **2023**, *13*, 2416. [CrossRef] [PubMed]
34. Liao, G.; He, Y.; Wang, H.; Fang, B.; Tsubaki, N.; Li, C. Carbon neutrality enabled by structure-tailored zeolite-based nanomaterials. *Device* **2023**, *1*, 100173. [CrossRef]
35. Fang, B.; Daniel, L.; Bonakdarpour, A.; Govindarajan, R.; Sharman, J.; Wilkinson, D.P. Dense Pt Nanowire Electrocatal. Improv. Fuel Cell Perform. Using A Graph. Carbon Nitride-Decor. Hierarchical Nanocarbon Support. *Small* **2021**, *17*, 2102288. [CrossRef]
36. Zhang, Y.; Zhou, W.; Peng, W.; Yao, T.; Zhang, Y.; Wang, B.; Cai, H.; Li, B. Core@Double–Shell Engineering of Zn Particles toward Elevated Dielectric Properties: Multiple Polarization Mechanisms in Zn@Znch@PS/PVDF Composites. *Macromol. Rapid Commun.* **2024**, *45*, 2300585. [CrossRef] [PubMed]
37. Fang, B.; Kim, J.H.; Kim, M.-S.; Yu, J.-S. Hierarchical Nanostructured Carbons with Meso–Macroporosity: Design, Characterization, and Applications. *Acc. Chem. Res.* **2013**, *46*, 1397–1406. [CrossRef]
38. Zhang, F.; Tang, N.; Jiang, Q.; Qi, K.; Zhu, X.; Luo, Z.; Kong, X.; Zang, D.; Liu, H.; Fang, B. Progress in polyacrylate-based electrically conductive adhesives: Featured properties, preparation, applications, and perspectives. *Polym. Compos.* **2024**, *45*, 5781–5803. [CrossRef]
39. Zhang, Z.; Zhou, J.; Zhou, X.; Wang, C.; Pan, Z.; Xu, X.; Liu, X.; Wang, Z.; Wu, Y.; Jiang, S.; et al. Graphene oxide-supported $MnV_2O_6$ nanoribbons with enhanced electrochemical performance for sodium-ion batteries. *J. Power Sources* **2024**, *597*, 234117. [CrossRef]
40. Zhang, Y.; Zhang, Z.; Yu, S.; Johnson, H.M.; Zhao, D.-C.; Tan, S.-C.; Pan, Z.-D.; Wang, Z.-L.; Wu, Y.-T.; Liu, X. Three-dimensional nanostructured $Co_2VO_4$-decorated carbon nanotubes for sodium-ion battery anode materials. *Rare Met.* **2023**, *42*, 4060–4069. [CrossRef]
41. Jiang, X.; Li, X.; Kong, Y.; Deng, C.; Li, X.; Hu, Q.; Yang, H.; He, C. A hierarchically structured tin-cobalt composite with an enhanced electronic effect for high-performance $CO_2$ electroreduction in a wide potential range. *J. Energy Chem.* **2023**, *76*, 462–469. [CrossRef]

42. Li, J.; Liu, X.; Zhao, H.; Yang, X.; Xiao, S.; Liu, N.; Zhao, N.; Cao, Y.; Yu, X.; Li, X. Dual-Phase engineering of $Ni_3S_2$/NiCo-MOF nanocomposites for enhanced ion storage and electron migration. *Chem. Eng. J.* **2024**, *489*, 151069. [CrossRef]
43. Ding, S.; An, J.; Gao, Y.; Ding, D.; Lu, X.; Zhao, L. Electrochemical performance of all-solid-state asymmetric supercapacitors based on Cu/Ni-Co $(OH)_2/Co_4S_3$ self-supported electrodes. *Chem. Eng. J.* **2023**, *453*, 139714. [CrossRef]
44. Senokos, E.; Anthony, D.B.; Rubio, N.; Ribadeneyra, M.C.; Greenhalgh, E.S.; Shaffer, M.S. Robust single-walled carbon nanotube-infiltrated carbon fiber electrodes for structural supercapacitors: From reductive dissolution to high performance devices. *Adv. Funct. Mater.* **2023**, *33*, 2212697. [CrossRef]